Research Article

Yonghao Zhao* and Yanglin Gu

Deformation mechanisms and plasticity of ultrafine-grained Al under complex stress state revealed by digital image correlation technique

Abstract: Conventional engineering stress–strain curve could not accurately describe the local deformability of the tensile necking part because the strain is calculated by assuming that the tensile specimen was deformed uniformly. In this study, we used 3D optical measuring digital image correlation to systematically measure the full strain field and actual flow stress in the necking region of ultrafine-grained (UFG) Al. The post-necking elongation and strain hardening exponent of the UFG Al were measured as 80% and 0.10, slightly smaller than those of the coarse-grained Al (117% and 0.28), suggesting the high plastic deformability of the UFG Al under complex stress state. Microstructural studies revealed the shear and ductile fracture, numerous micro-shear bands, and elongated UFG grains in the UFG Al, which are controlled by cooperative grain boundary sliding and multiple dislocation slips.

Keywords: nanostructured metals, plasticity, plastic deformation mechanisms, localized necking, complex stress state

1 Introduction

Bulk ultrafine-grained (UFG) metals with grain sizes smaller than 1 μm made *via* severe plastic deformation typically have high strength but very low tensile ductility at ambient temperatures [1–7]. This is not surprising because they are derived from excessively cold worked metals. Therefore, during tensile test, the UFG metals are susceptible to plastic instabilities such as necking because of their low dislocation accumulation capability and null strain hardening capability. The onset of localized deformation, *i.e.*, necking instability, is predicted by the Considere criterion:

$$\left(\frac{\partial \sigma}{\partial \varepsilon}\right)_{\dot{\varepsilon}} \leq \sigma, \tag{1}$$

where σ and ε are true stress and true strain, respectively, and $\dot{\varepsilon}$ is the strain rate. For the UFG materials, their strength at the right-hand side of equation (1) is high and strain hardening rate at the left-hand side of equation (1) is low, making it easy for premature necking even at small tensile strain. As a result, their tensile stress–strain curves peak quickly after yielding and then drop till fracture because of strain localization.

Because the UFG materials have a propensity for strain localization, the low ductility of the UFG materials may limit their applications. Many investigators tried to enhance the ductility of the UFG materials by increasing the storage capacity of dislocation. Those strategies are mostly based on either changing the testing conditions (such as strain rate and/or temperature [8,9]) or designing microstructures (such as formation of bimodal microstructure [10,11], introduction of second phase precipitates [12], *etc.*). However, not much attention has been paid on the effect of the stress state. Some results have shown that the stress state may also affect the strain hardening behavior [13,14]. Up to now only a few investigations have focused on the effect of the UFG microstructure on sheet formability, in which the UFG material is deformed in the multi-axial mode along a complex strain path. These studies suggest that even though the UFG sheet materials show very limited deformability in the tensile test, their formability in stretch forming was relatively good [15,16]. However, there is no systematic study on the plasticity and deformation mechanisms of the UFG

* **Corresponding author: Yonghao Zhao,** Nano and Heterogeneous Materials Center, School of Materials Science and Engineering, Nanjing University of Science and Technology, Nanjing 210094, China, e-mail: yhzhao@njust.edu.cn
Yanglin Gu: Nano and Heterogeneous Materials Center, School of Materials Science and Engineering, Nanjing University of Science and Technology, Nanjing 210094, China

materials under the complex stress state. Here the influence of complex stress state on the mechanical behavior of the UFG materials will be explored by focusing on the post-necking deformation during tensile test, which deformed under the complex stress state.

When necking instability occurs, deformation is concentrated in the local part, and the stress state of the necking part was transformed from uniaxial to multiple axial stress state. Therefore, the necking deformation in tensile testing provides an excellent opportunity for us to reveal the intrinsic deformation behavior of UFG metals under complex stress state. Because of rapid strain localization and the complex geometry of the neck, it is challenging to determine the real-time actual flow stress and local strain during the whole necking process in tensile tests, which hinder the measurements of real strain hardening ability and plasticity of the UFG materials under complex stress state [17]. Here we demonstrated direct visualization of the necking process by 3D optical measuring digital image correlation (DIC) techniques. The ARAMIS software invented by GOM provides real-time results for multiple measurement positions on the tensile specimen surface. This technology is useful to measure the full strain field and local strain during the whole tensile process, and therefore it was used to calculate the real-time strain and actual flow stress in the necking region.

The objectives of this study are two aspects: first, to explore a new approach that can be used to describe the actual flow stress and strain hardening behavior of the necking region of the UFG materials; second, to study the mechanical properties and deformation mechanisms of the UFG materials under the complex stress state.

2 Materials and experimental procedures

2.1 Sample preparation

Commercially pure 1050 Al (99.578 wt%) was chosen as a model material in this investigation, and its chemical compositions are listed in Table 1. The coarse-grained (CG) Al was obtained by annealing at 400°C for 2 h in the atmosphere of nitrogen. The CG Al 12 mm × 12 mm square bars were then processed by equal-channel angular pressing (ECAP) technique at ambient temperature using route A for eight passes to achieve their UFG structure. In route A, the sample was not rotated between adjacent passes. The

Table 1: Measured chemical composition (wt%) of the as-received commercially pure 1,050 Al by inductive coupled plasma emission spectrometer and ONH analyzers

Elements	Mg	Zn	Cu	Fe	Al	Si	Al
wt%	0.004	0.009	0.001	0.31	0.008	0.09	99.578

ECAP die has an L-shaped channel with an intersecting channel angle of 90° and an outer-arc angle of 45°. An effective strain of approximately one was imposed per ECAP pass, respectively.

2.2 Tensile test and DIC technique

For the tensile test, the UFG and CG Al samples were turning machined into dog-bone plate shape with a gauge dimension of ϕ 4 mm × 10 mm. Tensile direction was parallel to the ECAP extrusion direction. Tensile tests were run on a $w + b$ LFM20KN testing machine (Walter + Bai AG in Switzerland) in quasi-static loading at a strain rate of $10^{-4}\,s^{-1}$ at room temperature. Three identical samples were repeated for both CG and UFG Al, and we obtained a good repetition. In each tensile test, the strain was measured by 3D optical measuring techniques (GOM company in Germany). To evaluate the strain, the surface of the specimen was covered by black and white paints and formed random patterns. These patterns were created by spraying a background of flexible, adhesive, matte white paint on a previously degreased specimen. A thin layer of spots of black paint was then sprayed onto the white background [18,19]. Figure 1 schematically represents the measurement theory of local longitudinal and transversal strains ($\varepsilon_X = (L - L_0)/L_0$ and $\varepsilon_Y = (B - B_0)/B_0$), respectively. Two charge coupled device cameras with a certain angle were used to take real-time digital images in the gauge length during the entire tensile testing. The recorded images were then analyzed by ARAMIS software to obtain the displacements of the corresponding point by correlating the gray level of both the reference and comparative images. To get the strain distribution in the gauge length during the tensile process, the definitions of a facet size, which depends on the pattern applied to the specimen surface, and a facet step, which defines the distance between two facet center points, are required as 19 and 15 pixels, respectively. The image resolution is 2,352 × 1,728 pixels, and the strain window size is 30 mm × 24 mm. As the gray value of each facet is different, the whole field and local strains can be obtained by tracking the area with the same gray value in
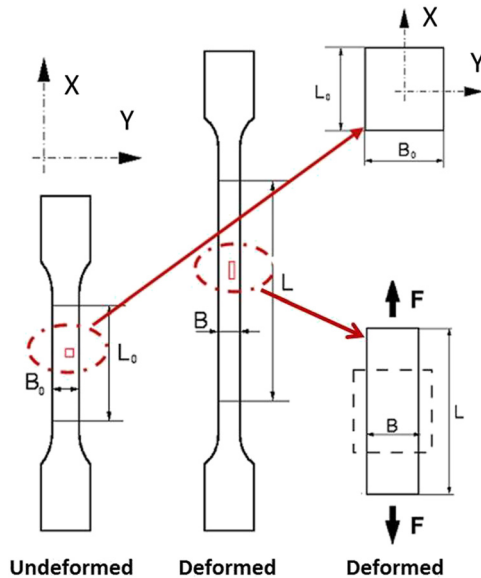
Figure 1: Schematic representation of 3D optical measuring DIC techniques to measure the full strain field and local longitudinal and transversal strains $\varepsilon_X = (L - L_0)/L_0$ and $\varepsilon_Y = (B - B_0)/B_0$, respectively.

temperature, respectively. EBSD scans were performed using Oxford system on the FEI SEM apparatus with step sizes of 60 nm.

The TEM observations of UFG Al were carried out on a Philips CM12 microscope operated at 100 kV. To prepare TEM specimens, the UFG Al samples were prepared by first mechanically grinding the samples to a thickness of about 50–70 μm, then dimpling to a thickness of about 20 μm, and finally ion milling to a thickness of electron transparency using a Gatan Precision Ion Milling System with an Ar^+ accelerating voltage of 4 kV and a temperature below 35°C. Important information about ductile damage evolution and fracture mechanisms can be gathered by scanning electron microscope (SEM).

the stretching process. Load/stress data were acquired as a function of time from the tensile testing machine and then imported to the ARAMIS software. The two measurements were correlated to obtain the stress–strain plot of the specimen.

2.3 Microstructure characterization

Microstructures of the UFG Al samples were characterized using electron backscattered diffraction (EBSD) and transmission electron microscope (TEM). The UFG Al samples for EBSD were first polished using diamond suspension with particle diameter of 6, 3, and 1 μm in turn, and then electropolished in a solution of 10% perchloric acid and 90% ethyl alcohol at 25 V for 10 s at cryogenic

3 Results

3.1 Microstructures of UFG Al

The microstructures of the UFG Al are shown in Figure 2. Figure 2a shows EBSD inverse pole figure (IPF) orientation mappings of UFG Al [20]. It is apparent that the plastic deformation induced by ECAP in UFG Al was not uniform, resulting in a mixture of micron and sub-micron-sized grains. The as-ECAP'ed Al sample is composed of equiaxed grains with sizes ranging from about 100 nm to 2 μm and an average size of about 740 nm (Figure 2c). Moreover, there are numerous fine sub-micron grains (with a size less than 250 nm) distributed at the GBs of micrometer or sub-micrometer grains. These microstructural features are consistent without previous investigation [20]. The fine sub-micrometer grains are likely to have formed as a result of dynamic recrystallization during ECAP processing, as verified by TEM results presented in Figure 2b. TEM observations indicated that statistically
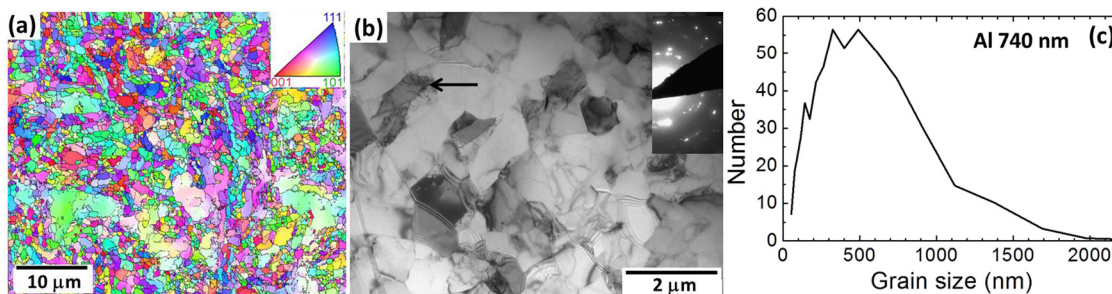
Figure 2: (a) EBSD IPF orientation mappings of the UFG Al [20]. The insets in (a) are the IPF color code scheme. (b) TEM image of the UFG Al. The inset is selected-area electron diffraction patterns. (c) The grain size distribution histograms of the UFG Al.

stored dislocations (such as tangled dislocations, dislocation forests, and discrete single dislocations) were occasionally observed in grains (marked by black arrow in Figure 2b). Most grains are thought to form as a result of recrystallization because of their large orientation differences from their surrounding matrix and dislocation free. The ring-like SAD pattern shows that the grain boundaries are mainly of a high-angle type and grains are randomly oriented. It suggests that the restoration occurs to some degree during the ECAP process, which can be attributed to accumulated strain and adiabatic heating because of large plastic deformation. The higher accumulated strain after eight passes corresponds to the larger driving force for recovery and short-range GB migration. The non-uniform deformation of UFG Al might be caused by route A because the other ECAP routes (b and c) with eight passes could produce uniform microstructures of UFG Al [2].

3.2 Tensile behavior of the UFG Al

Figure 3 shows the measured strain field contour maps and true local major strains along tensile axis at seven levels of global major engineering strain ε in the whole gauge length of the UFG and CG Al, respectively. For the CG Al, at the beginning of loading when ε = 10.022%, the specimen was deformed homogeneously throughout the entire gauge length. With increasing ε up to 20.934%, the deformation is gradually extended to the whole tensile sample because of strain hardening effect of the CG Al. When ε = 32.889%, the load reaches its maximum, stress concentration was triggered, and deformation became localized. From Figure 3d, one can see that the distribution of the true major strain is not uniform in the necking part but exhibits a peak with maximum value in the necking center. When ε = 51.848%, i.e., a major strain near fracture, the maximum true major strain in the necking part can be as high as 150%. Different from the CG Al, the deformation of the UFG Al is concentrated in the middle of the tensile specimen from 2.947% global strain until fracture, as shown in Figure 3a. The true major strain evolution of the UFG Al in Figure 3c further verified the above deformation feature. Moreover, the true major strain in the necking part also exhibits a peak distribution with a maximum value of 100% when ε = 24.287% (near the sample broken point). As the strain continues to evolve in the localized region, ARAMIS software cannot resolve the extremely high strain because of the destruction of the speckles. Therefore, the local strains at the failure initiation site are somewhat higher

than the strain obtained by the software at the last frame [21].

Combining the global major engineering strain ε with the measured load value together, we can easily obtain the traditional engineering stress–strain curves of the CG and UFG Al, as shown in Figure 4. The CG Al has a yield strength of 51 MPa, an ultimate tensile strength of 85 MPa, a uniform elongation of 28%, as well as an elongation to failure of 58%. The UFG Al has a high yield strength of 165 MPa and the ultimate tensile strength of 185 MPa but a very low uniform elongation of 2% and a ductility of 26%. For the UFG Al, necking occurred quickly after yielding, agreeing with the above-measured strain field contour maps in Figure 2. Therefore, the low overall tensile ductility of the UFG Al was mainly caused by its almost missing uniform elongation. The premature necking instability of the UFG Al was explained by its nearly null strain hardening capability [22]. The ECAP processing consumed the strain hardening capability by saturating dislocation accumulation; therefore, further dislocation accumulation and strain hardening become difficult during subsequent tension. However, different from the huge differences in uniform elongation between the UFG and CG Al, the post-necking elongation of the UFG Al (26%) is slightly smaller than that of the CG Al (30%), hinting a strong deformability of the UFG Al in the necking part. In addition, after necking onset, the uniform deformation of the whole gauge part of the material changes to the local deformation of the necking region, and the other parts outside the necking region are no longer deformed and enter the "frozen" state, so it is unreasonable to calculate the strain with the whole gauge part because it cannot accurately reflect the local deformation capacity of the material after necking. Or put it another way, the measured engineering stress–strain curves could not describe the true stress–strain of the necking part accurately because it assumes the tensile specimen was deformed uniformly. This makes us to re-examine the stress–strain curve of necking part by 3D optical measuring techniques.

To compare the plastic capability of the UFG and CG Al after uniform deformation, only the necking stage needs to be taken into consideration. ARAMIS software can give the local strain evolution of each point on the tested sample, which is effective to define the necking region. Figure 5 is a snapshot from the measured video of the UFG Al at stage 329 and time of 164.50 s (Supplementary Video: DIC-UFG Al and DIC-CG Al). Figure 5b and c show the real-time true major strain variations of five points with numbers of 0, 1 up to 5 on the UFG Al tensile specimen during the tension. At the beginning,
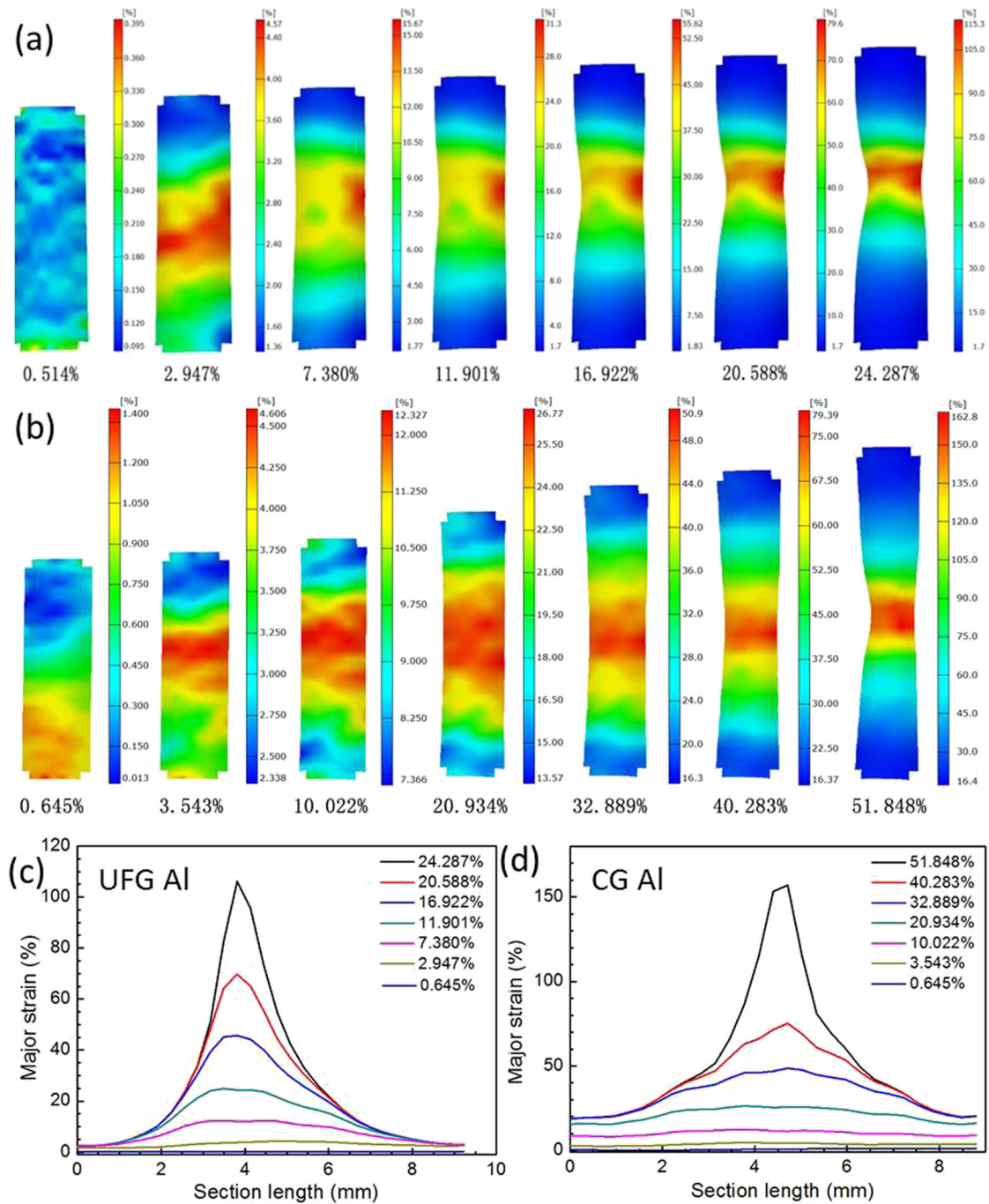
Figure 3: Strain field contour maps (a and b) and true local major/longitudinal strain ε_X (c and d) at seven levels of global engineering strain in the whole gauge part of the UFG (a and c) and CG (b and d) Al, respectively.

the major strain uniformly increases with the time in the whole gauge length. However, after a certain instant, the strain begins to concentrate within a local part and the major strain in the local part (points 2 and 3) rises up exponentially. The strains of points 1 and 4 increase monotonically until fracture, while the strain of point 0 ceases to increase and even undergoes elastic unloading immediately before the final fracture, showing a downward trend. It can be inferred that points 1 and 4 are located in the necking instability region, while point 0 is located in regions outside but close to the necking zone [19]. The actual gauge length for the necking part can be determined by selecting two points most adjacent to the strain localization zone and defining the region between
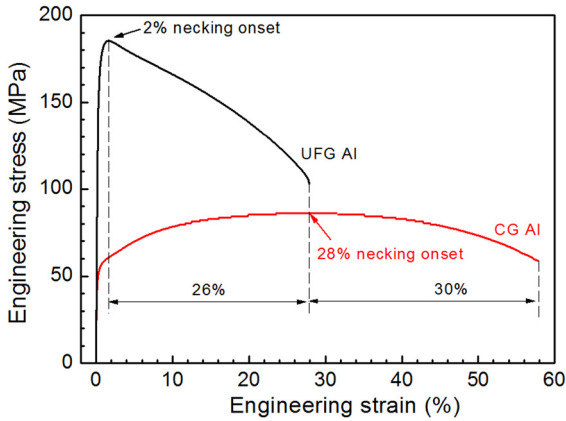
Figure 4: Global engineering stress–strain curves of the UFG and CG Al.

the two points as the necking region. The neck lengths of the UFG and CG Al specimen are 2.748 and 3.459 mm, respectively. The CG Al shows slightly higher resistance to the necking deformation because of its higher strain hardening ability, making the necking deformation distributing in a large range than the UFG Al.

The calculated major strain based on the actual gauge length of the necking part was then called apparent strain. Obviously, the apparent strain is a global average of the local longitudinal strain in the necking part, and it is more accurate than the nominal engineering strain. In the same way, because the necking region is becoming thinner, the

engineering stress, calculated by dividing the load by the initial cross-section area, cannot accurately reflect the real stress change in the necking region [23]. Here we divided the axial tensile load by the minimum cross-sectional area in the necking region to calculate the apparent stress. Obviously, the apparent stress represents the maximum true stress in the necking region and is more accurate than the nominal engineering stress. Then we get the apparent stress–strain curves of the UFG and CG Al in the necking part, as shown in Figure 6. First, for both UFG and CG Al, the apparent stress increases with increasing apparent strain, suggesting there exists strain hardening during the necking deformation of the UFG Al. Strain hardening exponent n is a parameter used for evaluating strain hardening capability, and its values, simulated by the Hollomon equation [24], are 0.10 and 0.28 for the UFG and CG Al, respectively. Second, at the end of the stretch curve, there is still a downward drop, which may be caused by the inner voids in the necking part at the later stage of necking near the fracture. In this stage, the apparent stress could not reflect the maximum true stress anymore. Third, considering the CG Al has a large uniform tensile strain of 28%, the elongation of the necking region for the CG Al should be calculated by subtracting the uniform elongation and is ~117%. The post-necking elongation of the UFG Al is calculated as 80%, which is greatly larger than traditionally measured value (26%), as listed in Table 2. The post-necking elongation of the UFG Al is
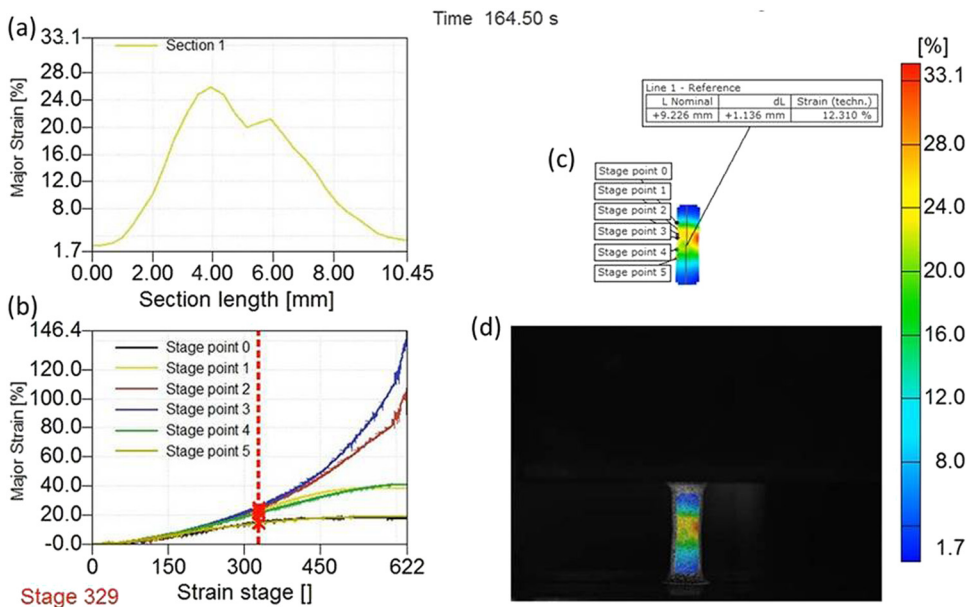
Figure 5: A snapshot from the measured video of the UFG Al at stage 329 and time of 164.50 s; (a) true local major/longitudinal strain ε_x in the whole gauge part; (b) true major/longitudinal strain evolutions of five points near necking zone in the UFG Al during tensile test; (c) positions of the five points near necking zone in the UFG Al during tensile test in (b); and (d) image of whole gauge part of the UFG Al.
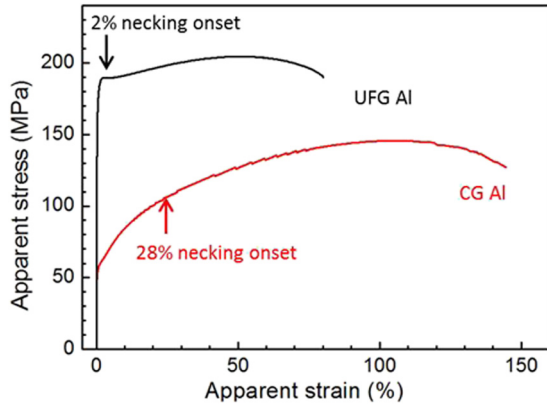
Figure 6: Apparent stress–strain curves of the UFG and CG Al in the necking region.

slightly smaller than that of the CG Al (117%), suggesting a large deformability of the UFG Al in the necking part. It can be found that despite the great difference between the UFG and CG Al in their engineering stress–strain curves, there is no big difference between post-necking elongations of the UFG and CG Al. Considering the deformation under the complex stress state, it can be inferred that the UFG Al has relatively good plasticity under multi-axial stress state.

The strain hardening exponent reflects the ability of metal materials to resist uniform plastic deformation. The strain hardening characteristics of the material continue to play a role in the process of resistance to plastic instability. Because of the high strain hardening exponent of the CG Al, it shows a high resistance to the deformation localization in the necking process, and the necking deformation is distributed in a large range. Therefore, the necking deformation is more diffuse and the neck contour opening is wider. Because of the low strain hardening exponent of UFG Al, the necking deformation is relatively loose. The development of necking process and the localization resistance of necking deformation are low. Therefore, the distribution of necking deformation is concentrated and the opening of neck contour is small. The elastic modulus E and Poisson's ratio v of the UFG Al are slightly smaller than those of the CG Al, as listed in

Table 2. The former was caused by large volume fraction of GBs in the UFG Al, and the latter was caused by slightly low deformability of the UFG Al.

3.3 Ductile fracture surface

To further understand the tensile properties and build the relationship between microstructures and mechanical behavior, we studied the surface morphology and fracture mode using the SEM. Figure 7 shows SEM images of the macro- and micro-scale fracture surfaces of the UFG and CG Al samples, respectively. The CG Al sample fractured *via* a ductile mechanism with a larger area reduction of fracture surface of 93.3% and the numerous dimples over the entire fracture surface. From the micro-scale SEM images in Figure 7d, homogeneously distributed honeycomb-like dimples were observed having an average size larger than 10 μm. Moreover, the dimples are elongated because of void nucleation and subsequent coalescence *via* shear fracture, as revealed below and discussed in Section 4.2.

For UFG Al, the fracture surface is rough with a high concentration of uneven concave. A close examination of the concaves in the fracture surface revealed a large number of homogeneously distributed honeycomb-like dimples. Careful inspection showed that the dimples include two types: one has an average size in a range of several micrometers and the other has an average size of larger than 10 μm, as shown in micro-scale SEM image in Figure 7b. Although the size of the dimples is smaller compared to CG Al, they can also provide ability of ductile deformation. In fact, the UFG Al indeed fractured in a ductile manner, as evidenced by a large area reduction in fracture surface of 82.4%. The larger fracture area reduction and dimple size of the CG Al than those of UFG Al indicate its larger deformability. It is believed that the dimples are initiation sites for fracture. In the literature, Kumar *et al.* give three hypothetical mechanisms responsible for void initiation in fully dense UFG materials, and the spacing of these initiation sites determines the dimple size [25].

Table 2: Lists of yield strength $\sigma_{0.2}$, ultimate tensile strength σ_{UTS}, uniform elongation ε_{ue}, post-necking elongation ε_{pe}, elongation to failure ε_{ef}, gauge length of necking region l_0, apparent elongation at necking ε_{ae}, strain hardening exponent n, elastic modulus E, Poisson's ratio, v of the UFG and CG Al

	$\sigma_{0.2}$ (MPa)	σ_{UTS} (MPa)	ε_{ue} (%)	ε_{ef} (%)	ε_{pe} (%)	n	ε_{ae} (%)	l_0 (mm)	E (GPa)	v
CG	51	85	28	58	30	0.28	117	3.459	71	0.33
UFG	165	185	2	28	26	0.10	80	2.748	69	0.31
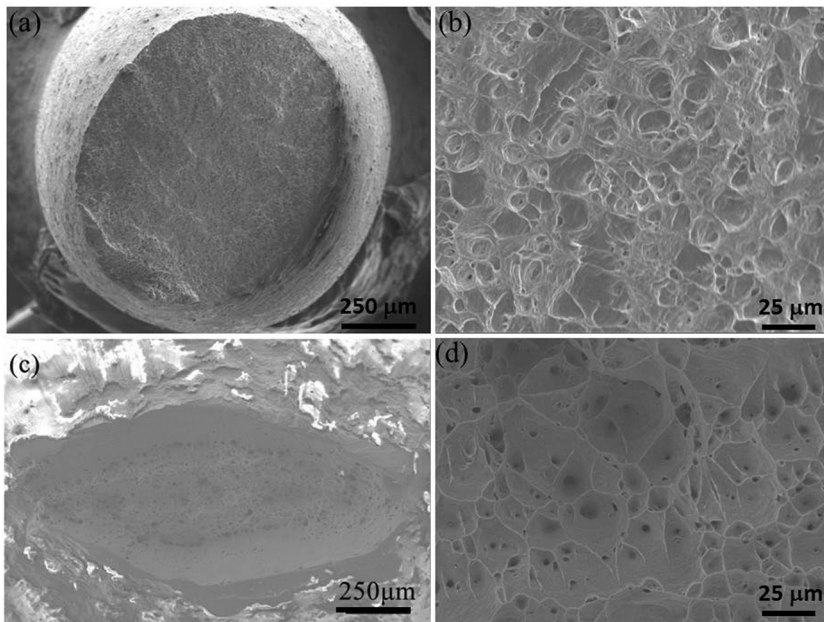
Figure 7: SEM images of the fracture surfaces of the UFG (a and b) and CG Al (c and d); (a and c) low magnification; and (b and d) high magnification.

3.4 Shear fracture and surface relief

Figure 8 shows the SEM images from side view of the CG and UFG Al, respectively. The UFG sample failed in a shear fracture mode with a shear fracture angle θ (the angle between the fracture surface and tension axis) of about 64°. However, the CG Al fractured in a normal way with $\theta = 90°$. During the uniform deformation, the strain
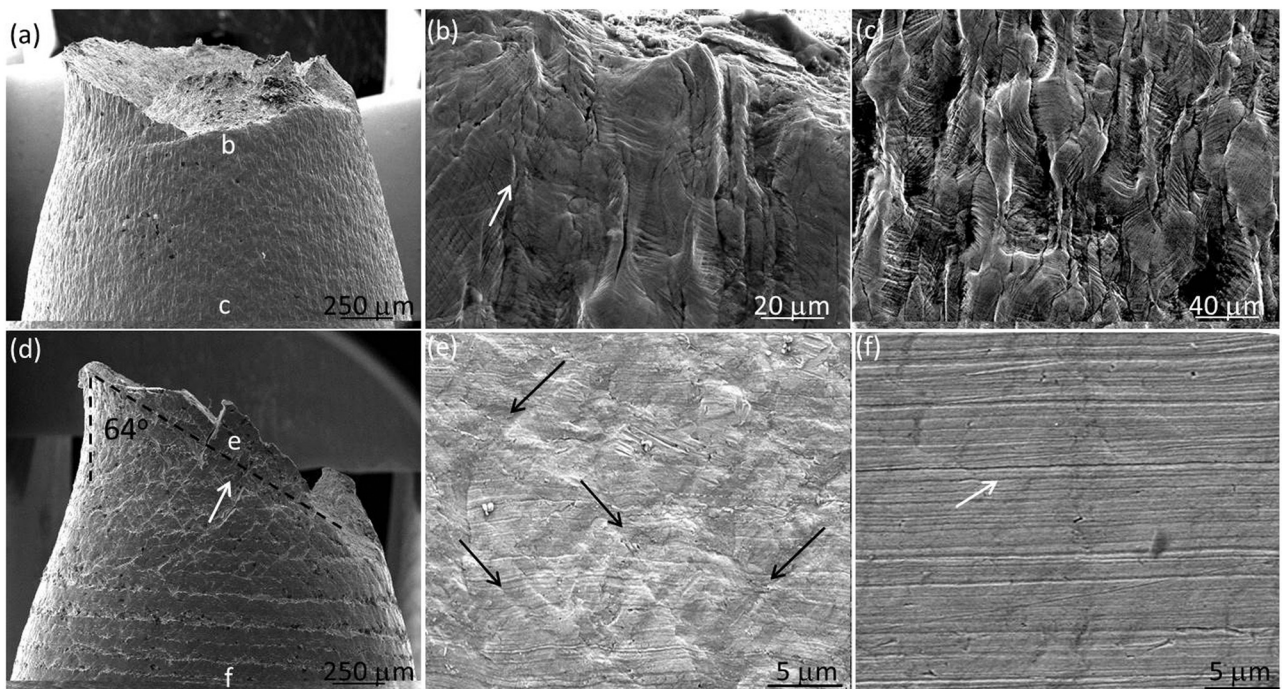
Figure 8: Face-view SEM images of the fractured tensile specimens of the CG (a–c) and UFG Al (d–f); (b) and (c) are the magnified images of the necking region near the fracture marked as "b" and the uniform deformed region marked as "c" in (a), respectively; (e) and (f) are the magnified SEM images of the regions marked as "e" and "f" in (d), respectively.

path is along the direction of the maximum shear stress, *i.e.*, the shear angle is 45°. When necking occurs, the maximum strain path was changed, and the fracture angle will be slightly increased. The deviated shear fracture angle from 45° of the CG and UFG Al indicated again that necking occurs in both samples, and the CG Al exhibits a greater degree of deviation because of its higher strain hardening ability. From fracture mechanics, the larger shear fracture angle than 45° of the CG and UFG Al indicates that the fracture behavior is controlled by both normal stress and shear stress on the shear fracture surface [23], as calculated and discussed in Section 4.2 in detail.

To study the mechanisms operating during plastic deformation under the complex stress state, the surface relief of pre-polished fractured specimens was carefully inspected in SEM. Figure 8b, c, e, and f shows the microscale surface relief SEM images from face view of the CG and UFG Al. For the CG Al, the surface relief in the homogeneous plastic deformation area is similar to the necking region, revealing that CG Al was deformed by dislocation slip under both uniaxial and multi-axial stress state (Figure 8b and c). For the CG Al, at the initial stage of deformation, grains with maximum shear stress on slip systems begin to slide first. The sliding of dislocations is then blocked and accumulated by GBs, forming a ridge at GBs. With the stress increase, multiple dislocation slips are activated and further slide in the deformed grains, causing the increase in stress concentration at the boundary. The deformed CG grains are then elongated with the help of numerous dislocation slip bands. When the stress reaches a certain degree, the dislocations slip systems in neighboring grains are excited. The slip bands in the adjacent grains are blocked at GBs and forming ridges at GBs (pointed by white arrow in Figure 8b). Because the critical slip shear stress of CG Al dislocation is small, the deformation is easy to transfer from one grain to another, so that more and more grains participate in the sliding, resulting in large plastic deformation of the sample.

For the UFG Al, the surface relief in the necking area has much higher roughness than the uniform deformed region (Figure 8e and f). Careful observation on the sample surface revealed the numerous rough localized plastic deformation markings or traces with about 45° to tensile direction in the necking region on the fractured specimen, as pointed by black arrows in Figure 8e. However, there are no such deformation markings or traces at the region far away from the necking part, as shown in Figure 8f, which indicated that the deformation markings near fracture were formed during necking deformation.

The parallel markings as pointed by white arrow in Figure 8f are the traces left by the turning tool when turning the tensile specimens. Several published studies reported similar deformation traces in UFG Al [26], 6,082 Al alloys [27], Ni and Cu [23], which were described as microscopic or mesoscopic shear bands or shear planes. From Figure 8e and f, the distances between shear bands are several micrometers, and the lengths of the shear bands extend from several micrometers to several 10 μm. The size of the shear bands is much larger than the grain size of the UFG Al (~220 nm), suggesting cooperative GB sliding may involve in the plastic deformation, which was further revealed below and discussed in Section 4.3.

3.5 Postmortem microstructures at necking region

To further study the mechanisms operating during plastic deformation under the complex stress state, EBSD characterization was used to comparably analyze the microstructures in the necking region near fracture and the region of uniform deformation (far away from the necking) of the UFG Al after fracture, as shown in Figure 9. It can be seen that the grain size and morphology in the region far away from the necking area has no obvious change compared with those of the initial UFG Al (Figure 2a). However, the grains in the necking area are obviously elongated along the tensile direction (Figure 9b), indicating dislocation slip also contributes to the large plastic deformability of UFG Al under the complex stress. This is a direct evidence for the activation of more slip system in the necking region of the UFG Al under 3D stress state, because the elongated UFG grains can be achieved only through the initiation of multiple slip systems in the UFG grains. The further more dislocation slips enhance the plastic deformation ability of the UFG Al in the necking region, as further discussed in Section 4.

4 Discussion

A large number of previous literature shows that the plastic deformation ability of UFG material is much lower than that of CG counterparts. However, the conventionally measured engineering stress–strain curves could not describe the true stress–strain of the necking part accurately because it assumes the tensile specimen was deformed uniformly. In this work, we used DIC technique
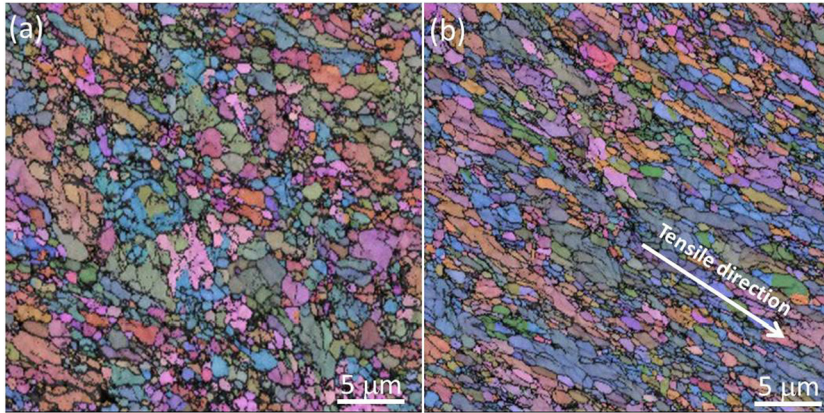
Figure 9: (a) EBSD image of the uniform deformed region of the UFG Al. (b) EBSD image of the necking region near the fracture of the UFG Al. The tensile direction was pointed out by the white arrow.

to accurately measure the full strain field as well as local strain during the whole tensile process. Our results indicated that the plastic deformability in the necking part of the UFG Al is only slightly smaller than that of CG counterpart. Postmortem observation revealed the tendencies of shear and ductile fracture, and numerous micro-shear bands and elongated UFG grains in the UFG Al. In the following, the abovementioned results from the aspects of deformation mechanisms and fracture mechanics will be discussed.

4.1 Necking: nonlinear section shrinkage and influence factors

Necking is the phenomenon of specimen cross-sectional reduction during tension and is a joint action of hardening and weakening mechanisms. During uniform deformation before necking, the specimen elongation and section shrinkage are linear and conform to the condition of volume invariability. However, after necking, the specimen elongation is only borne by the necking region. To maintain the continuity of specimen under the control of the chuck, the necking region must be accelerated to shrink, and the section closer to the center of necking region will shrink faster, which is called nonlinear section shrinkage [23]. As revealed by DIC results in Figures 5 and 6b, the ε_X in the necking region of the CG Al increases exponentially after 800 s of loading.

The influence factors of necking include intrinsic characteristics of materials, such as n and m, and external deformation conditions, such as temperature, strain rate, and stress states. After necking, the strain hardening and

rate hardening mechanisms still work and further resist the necking process. The larger the n is, the greater the deformation resistance is. The strain rate sensitivity m indicates that the deformation resistance increases with the increase in strain rate. The higher strain rate leads to the increases in dislocation density and dislocation movement rate, $i.e.$, the increase in work hardening degree. Because both strain and strain rate at necking increase, large n and m values will result in further reinforcement of deformation resistance in the necking region, causing the unreinforced part to continue to deform. The positive n value (0.10) and large m (0.02 [28] in the UFG Al will expand the necking process and delay fracture, $i.e.$, enhance the plastic deformability of the necking region.

4.2 Shear fracture angle

For the plate tensile specimens, the final fracture mode is usually along the width or along the thickness direction with a shear angle under the combined action of normal stress and shear stress. At the same time, the shear angle is also related to the intrinsic plastic deformation ability of the material. As illustrated by the graphic representation in Figure 10a, if the tensile stress σ_T is imposed on the sample, the normal and shear stresses (σ_n and τ_s) on the shear plane with a shear angle θ can be expressed as:

$$\sigma_n = \sigma_T(1 - \cos^2\theta),\tag{2}$$

$$\tau_s = \sigma_T \sin\theta \cos\theta.\tag{3}$$

It can be seen from Figure 8b that when θ is less than 45°, σ_n is less than τ_s. When $\theta = 45°$, $\sigma_n = \tau_s$, and the fracture is generated under the maximum shear stress,
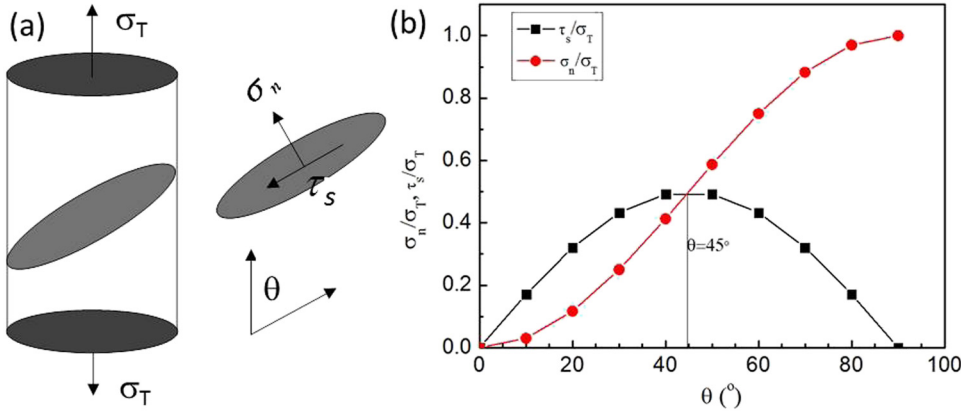
Figure 10: (a) Schematic representation of the normal and shear stresses (σ_n and τ_s) on the shear plane with a shear angle θ under tensile stress σ_T. (b) The variations in the normal and shear stresses against the shear angle θ.

which conforms to the Tresca fracture criterion. When θ is greater than 45°, $\sigma_n > \tau_s$, and the fracture is produced under the joint action of shear stress and normal stress. When $\theta = 90°$, σ_n reaches the maximum and $\tau_s = 0$, the fracture follows the maximum normal stress criterion.

Because the intrinsic shear strength of materials τ_0 is smaller than the cleavage normal breaking strength σ_0, during the uniform deformation, the strain path is along 45°, $i.e.$, the loading direction of the maximum shear stress. If there is no necking in the tensile process, the final θ is close to 45°. When necking occurs, the plastic deformation path of the material was changed, and the fracture angle will be increased over 45° [29,30]. The fracture angle and dimple size increase with the necking degree. For plate tensile specimen of ductile materials, shear fracture is the main fracture mode because the necking cannot reach the ideal degree before fracture. The deviated shear fracture angle from 45° of the CG and UFG Al indicated that necking occurs in both samples, and the CG Al exhibits slightly greater degree of necking process because of its higher strain hardening ability.

To better understand the shear angle and the shear fracture mechanism, Zhang $et~al.$ [23] proposed a unified tensile fracture criterion as follows:

$$\left(\frac{\sigma_n}{\sigma_0}\right)^2 + \left(\frac{\tau_n}{\tau_0}\right)^2 = 1. \tag{4}$$

According to the unified tensile fracture criterion, τ_0 and σ_0 can be calculated by the following equations:

$$\sigma_T = 2\tau_0\sqrt{1 - \alpha^2}, \tag{5}$$

$$\theta_T = \frac{\pi}{2} - \frac{1}{2}\arctan\left(\frac{\sqrt{1 - 2\alpha^2}}{\alpha^2}\right), \tag{6}$$

$$\alpha = \frac{\tau_0}{\sigma_0}, \tag{7}$$

where the ratio α is a fracture mode factor controlling the macro-scale fracture modes of a material. It is suggested that when $0 < \alpha < \sqrt{2}/2$, the shear fracture angle θ is in the range of 45–90° [23].

According to the unified tensile fracture criterion, the ratios α of the CG and UFG Al were calculated as 0.71 and 0.52, respectively. Their σ_0 and τ_0 were 99 MPa/70 MPa and 219 MPa/114 MPa, respectively. As shown in Table 3, σ_0 and τ_0 of the UFG Al are larger than those of the CG Al. The proportion of σ_0 to τ_0 in the UFG Al is also larger than that in the CG Al, resulting in a smaller ratio α and a smaller shear fracture angle. It has been demonstrated that the ECAP process can effectively change the fracture mode from normal fracture to shear fracture with different shear fracture angles [31].

4.3 Deformation mechanisms

Microstructure analysis found that stress mode does not affect the plastic deformation mechanisms of CG Al much, which is mainly dislocation glide (Figure 8b and c), while does affect those of the UFG Al (Figure 8d and f).

Table 3: Lists of fracture strength σ_F, shear fracture angle θ, ratio α, average critical normal fracture stress σ_0, and average critical shear fracture stresses τ_0 of the UFG and CG Al

Samples	σ_F (MPa)	θ (°)	A	σ_0 (MPa)	τ_0 (MPa)
CG Al	120	90	0.71	99	70
UFG Al	190	64	0.52	219	114
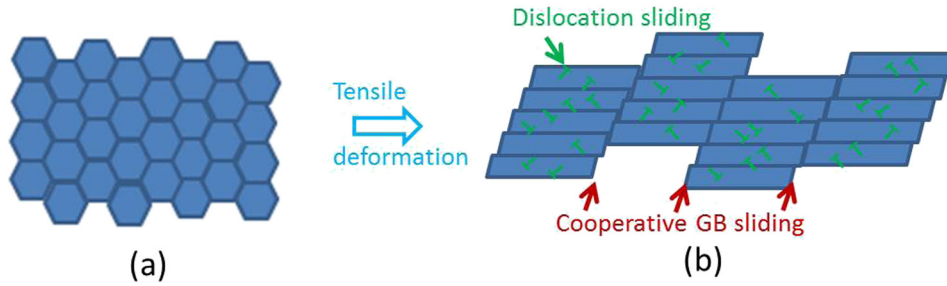
Figure 11: Schematic diagram of the deformation mechanism of UFG materials under the complex stress state: (a) initial microstructures; (b) tensile deformed microstructures with cooperative GB and dislocation sliding.

The UFG Al under uniaxial stress did not exhibit much deformation, while under triaxial stress in the necking region showed numerous micro-shear bands and elongated UFG grains. The underlying deformation mechanisms include GB sliding and multiple dislocation slips. In the past several decades, numerous investigations of experiments, molecular dynamic (MD) simulations, and other modeling efforts on deformation mechanisms of the nanocrystalline and UFG materials have revealed GB-mediated deformation such as grain rotation [32], GB sliding [33], GB diffusion [34], and stress-driven GB migration [35] besides the conventional slip of lattice dislocations [36]. Grain coalescence or growth usually occurred as a result of the above GB-mediated deformation [37]. In the sections that follow, we discuss each one within the context of the results described herein.

4.3.1 Grain boundary sliding

At elevated temperatures, GB sliding, *i.e.*, individual grains displaced with respect to each other along their mutual boundaries as a consequence of an external stress, is a well-established deformation process for CG materials [38]. The sliding of individual grains is accommodated either through the intra-granular dislocation slip or through the diffusional flow of vacancies [38].

The GB sliding of the UFG materials has been reported to occur even at room temperatures [33] because of the enhanced diffusion kinetics and/or stress-driven GB migration [35]. For the former reason, as suggested by the literature, even at room temperature, diffusion can play an important role in the plastic deformation of the UFG metals and alloys. The increased volume fraction of GBs promotes the GB diffusion processes because of enhanced diffusivity [39]. Moreover, high fractions of high-angle GBs and non-equilibrium GBs with many extrinsic dislocations lying in narrow regions adjacent

to the GBs have been frequently reported in the UFG materials. These boundaries and the associated high dislocation densities are probable to provide easy diffusive paths for the local re-arrangements needed to form the GB sliding. For the latter reason, stress-driven GB migration is also revealed as an athermal activation process by some *in situ* TEM observations [32]. The GB sliding is even observed to occur at very low temperature, such as at liquid nitrogen temperature [40].

4.3.2 Cooperative grain boundary sliding and micro-shear bands

Hahn *et al.* [41] proposed a theoretical model for the deformation of the UFG materials, *i.e.*, formation of mesoscopic glide planes based on the GB sliding. For the UFG materials, the high volume fraction of the GBs was argued to provide an opportunity for the formation of long planar interfaces by stretching over many grains and resulting in a macroscopic sliding over individual grain dimensions. Moreover, a cooperative GB sliding of the UFG materials was observed at ambient temperatures by *in situ* SEM and TEM observations [32]. In addition, the above mesoscopic shear planes and/or cooperative GB sliding are also revealed by MD and modeling computer simulations [33] as well as experiments [23]. A cooperative GB slide of a series of the UFG grains was observed in UFG Fe, Cu, Al, 6061 Al, and Ni [23–25].

In CG materials, the initial dimensions of micro-shear bands are significantly smaller than the coarse grain size because they are formed within a coarse grain. However, the micro-shear bands of the UFG metals are different from those seen in CG materials. The micro-shear bands in CG materials grow by spreading into neighboring grains across GBs and eventually form macro-shear bands. Such a relationship between the grain size and the dimensions of micro-shear band does not apply to the UFG

metals. Therefore, those shear bands in UFG metals, whose width/grain size ratio falls in the range of 1–10, are defined as micro-shear bands. They are distinct from the macro-shear bands which spread across the entire specimen cross section, form a fracture surface, and result in failure. The cooperative GB sliding and dislocation slip contributing the high plastic deformation of the UFG Al in the necking region under complex stress state is schematically shown in Figure 11.

5 Conclusions

In summary, the tensile testing with optical measuring DIC techniques is a powerful tool to study the deformation process during the tensile process. It can uncover mesoscopic deformation flow and reveal the details of the strain evolution on surface deformation, which is the footprint of underlying deformation mechanisms. In addition, SEM and TEM techniques were used to systematically investigate intrinsic plasticity and deformation mechanism of UFG Al at localized necking part with complex stress state. The detailed results are the following.

1. The UFG Al with an average grain size of 740 nm was achieved by ECAP.
2. DIC measurements indicated that for both UFG and CG Al, the apparent stress increases with increasing apparent strain in the necking region. Strain hardening exponents n are 0.10 and 0.28 for the UFG and CG Al, respectively. The elongation of the UFG Al in the necking region is 80%, slightly smaller than that of the CG Al (117%), suggesting a large deformability of the UFG Al in the necking part.
3. SEM and EBSD studies of fracture surface morphology of the UFG Al revealed the tendencies of shear and ductile fracture with a shear angle of 64°, and numerous homogeneous micro-shear bands as well as elongated UFG grains under triaxial stress state near fracture zone.
4. The deformation mechanism of the UFG Al strongly depends on the stress state. Cooperative GB sliding and multiple dislocation slips were active under the complex stress state at room temperature, which is contributed to the enhanced plasticity. Our work revealed the large plastic deformability of UFG metals under complex stress state.

References

[1] Koch CC, Youssef KM, Scattergood RO, Murty KL. Breakthroughs in optimization of mechanical properties of nanostructured metals and alloys. Adv Eng Mater. 2005;7:787–94.

[2] Valiev RZ, Estrin Y, Horita Z, Langdon TG, Zehetbauer MJ, Zhu YT. Producing bulk ultrafine-grained materials by severe plastic deformation: ten years later. JOM. 2016;68:1216–26.

[3] Wan YC, Bei T, Gao YH, Tang LL, Sha G, Zhang B, et al. Bulk nanocrystalline high-strength magnesium alloys prepared via rotary swaging. Acta Mater. 2020;200:274–86.

[4] Ni HT, Zhu J, Wang ZD, Lv HY, Su YY, Zhang XY. A brief overview on grain growth of bulk electrodeposited nanocrystalline nickel and nickel-iron alloys. Rev Adv Mater Sci. 2019;58:98–106.

[5] Muhamad SS, Ghani JA, Haron CHC, Yazid H. Cryogenic milling and formation of nanostructured machined surface of AISI 4340. Nanotech Rev. 2020;9:1104–17.

[6] Kong LB, Zhou YJ, Song KX, Hui D, Hu H, Guo BJ, et al. Effect of aging on properties and nanoscale precipitates of Cu–Ag–Cr alloy. Nanotech Rev. 2020;9:70–8.

[7] Yu H, Zhang LL, Cai FF, Zhong SJ, Ma J, Bao L, et al. Microstructure and mechanical properties of brazing joint of silver-based composite filler metal. Nanotech Rev. 2020;9:1034–43.

[8] Cheng S, Zhao YH, Guo Y, Li Y, Wei Q, Wang XL, et al. High plasticity and substantial deformation in nanocrystalline NiFe alloys under dynamic loading. Adv Mater. 2009;21:5001–4.

[9] Wang YM, Ma E, Valiev RZ, Zhu YT. Tough nanostructured metals at cryogenic temperatures. Adv Mater. 2004;16:328.

[10] Zhao YH, Topping T, Bingert JF, Dangelewicz AM, Li Y, Liu W, et al. High tensile ductility and strength in bulk nanostructured nickel. Adv Mater. 2008;20:3028.

[11] Zhao YH, Topping T, Li Y, Lavernia EJ. Strength and ductility of bi-modal Cu. Adv Eng Mater. 2011;13:865–71.

[12] Zhao YH, Liao XZ, Cheng S, Ma E, Zhu YT. Simultaneously increasing the ductility and strength of nanostructured alloys. Adv Mater. 2006;18:2280–3.

[13] Wu XL, Jiang P, Chen L, Yuan FP, Zhu YT. Extraordinary strain hardening by gradient structure. Proc Natl Acad Sci USA. 2014;111:7197–201.

[14] Lund AC, Schuh CA. Strength asymmetry in nanocrystalline metals under multiaxial loading. Acta Mater. 2005;53:3193–205.

[15] Taylor AS, Weiss M, Hilditch T, Stanford N, Hodgson PD. Formability of cryo-rolled aluminium in uniaxial and biaxial tension. Mater Sci Eng A. 2012;555:148–53.

[16] Moreno-Valle EC, Monclus MA, Molina-Aldareguia JM, Enikeev N, Sabirov I. Biaxial deformation behavior and enhanced formability of ultrafine-grained pure copper. Metall Mater Trans A. 2013;44A:2399–408.

[17] Yang K, Ivanisenko Y, Caron A, Chuvilin A, Kurmanaeva L, Scherer T, et al. Mechanical behaviour and in situ observation of shear bands in ultrafine grained Pd and Pd–Ag alloys. Acta Mater. 2010;58:967–78.

[18] Abbassi F, Nasri M, Brault R, Mistou S, Zghal A. An experimental and numerical study of necking initiation in biaxial tensile test. 15th International conference on experimental mechanics, Porto, Portugal, 22–27 July 2012.

[19] Martinez-Donaire AJ, Garcia-Lomas FJ, Vallellano C. New approaches to detect the onset of localised necking in sheets under through-thickness strain gradients. Mater Des. 2014;57:135–45.

[20] Zhao YH, Bingert JF, Topping TD, Sun PL, Liao XZ, Zhu YT, et al. Mechanical behavior, deformation mechanism and microstructure evolutions of ultrafine-grained Al during recovery via annealing. Mater Sci Eng A. 2020;772:138706.

[21] Ghahremaninezhad A, Ravi-Chandar K. Ductile failure behavior of polycrystalline Al 6061-T6. Int J Fract. 2012;174:177–202.

[22] Zhao YH, Zhu YT, Lavernia EJ. Strategies for improving tensile ductility of bulk nanostructured materials. Adv Eng Mater. 2010;12:769–78.

[23] Zhang Z, Hauge M, Ødegård J, Thaulow C. Determining material true stress–strain curve from tensile specimens with rectangular cross-section. Int J Solids Struct. 1999;36:3497–516.

[24] Courney TH. Mechanical behavior of materials. 2nd edn. New York, NY, USA: McGraw-Hill Companies, Inc.; 2000. p. 13.

[25] Kumar KS, Suresh S, Chisholm MF, Horton JA, Wang P. Deformation of electrodeposited nanocrystalline nickel. Acta Mater. 2003;51:387–405.

[26] Sabirov I, Estrin Y, Barnett MR, Almokhina I, Hodgson PD. Tensile deformation of an ultrafine-grained aluminium alloy: micro shear banding and grain boundary sliding. Acta Mater. 2008;56:2223–30.

[27] Vinogradov A, Hashimoto S, Patlan V, Kitagawa K. Atomic force microscopic study on surface morphology of ultra-fine grained materials after tensile testing. Mater Sci Eng A. 2001;319–23:862–6.

[28] Wei QM, Cheng S, Ramesh KT, Ma E. Effect of nanocrystalline and ultrafine grain sizes on the strain rate sensitivity and activation volume: fcc versus bcc metals. Mater Sci Eng A. 2004;381:71–9.

[29] Bai YL, Wierzbicki T. Application of extended Mohr-Coulomb criterion to ductile fracture. Int J Fract. 2010;161:1–20.

[30] Bai YL, Wierzbicki TA. Comparative study of three groups of ductile fracture loci in the 3D space. Eng Fract Mech. 2015;135:147–67.

[31] Fang DR, Duan QQ, Zhao NQ, Li JJ, Wu SD, Zhang ZF. Tensile properties and fracture mechanism of Al–Mg alloy subjected to equal channel angular pressing. Mater Sci Eng A. 2007;459:137–44.

[32] Shan ZW. Grain boundary-mediated plasticity in nanocrystalline nickel. Science. 2004;305:654–7.

[33] Yamakov V, Wolf D, Phillpot SR, Mukherjee AK, Gleiter H. Deformation-mechanism map for nanocrystalline metals by molecular-dynamics simulation. Nat Mater. 2004;3:43–7.

[34] Sergueeva AV, Mara NA, Mukherjee AK. Grain boundary sliding in nanomaterials at elevated temperatures. J Mater Sci. 2007;42:1433–8.

[35] Rupert TJ, Gianola DS, Gan Y, Hemker KJ. Experimental observations of stress-driven grain boundary migration. Science. 2009;326:1686–90.

[36] Wang JW, Narayana S, Huang JY, Zhang Z, Zhu T, Mao SX. Atomic-scale dynamic process of deformation-induced stacking fault tetrahedra in gold nanocrystals. Nature Commun. 2013;4:2340.

[37] Cheng S, Zhao YH, Wang YM, Li Y, Wang XL, Liaw PK, et al. Structure modulation driven by cyclic deformation in nanocrystalline NiFe. Phys Rev Lett. 2010;104:255501.

[38] Langdon TG. An evaluation of the strain contributed by grain boundary sliding in superplasticity. Mater Sci Eng A. 1994;174:225–30.

[39] Liddicoat PV, Liao XZ, Zhao YH, Zhu YT, Murashkin MY, Lavernia EJ, et al. Nanostructural hierarchy increases the strength of aluminium alloys. Nat Commun. 2010;1:63.

[40] Zhang K, Weertman JR, Eastman JAM. Rapid stress-driven grain coarsening in nanocrystalline Cu at ambient and cryogenic temperatures. Appl Phys Lett. 2005;87:061921.

[41] Hahn H, Padmanabhan KA. A model for the deformation of nanocrystalline materials. Philos Mag B. 1997;76:559–71.